

NASA TECHNICAL NOTE



NASA TN D-4864

0.1

LOAN COPY: RETURN
AFWL (WLIL-2)
KIRTLAND AFB, NM
0131604



NASA TN D-4864

SHOCK-WAVE PRESSURE DECAY IN POLYCARBONATE TARGETS IMPACTED BY CYLINDRICAL POLYCARBONATE PROJECTILES

by *John D. Di Battista*

Langley Research Center

Langley Station, Hampton, Va.

NATIONAL AERONAUTICS AND SPACE ADMINISTRATION • WASHINGTON, D. C. • NOVEMBER 1968



0131604

NASA TN D-4864

SHOCK-WAVE PRESSURE DECAY IN POLYCARBONATE TARGETS
IMPACTED BY CYLINDRICAL POLYCARBONATE PROJECTILES

By John D. Di Battista

Langley Research Center
Langley Station, Hampton, Va.

NATIONAL AERONAUTICS AND SPACE ADMINISTRATION

For sale by the Clearinghouse for Federal Scientific and Technical Information
Springfield, Virginia 22151 - CFSTI price \$3.00

SHOCK-WAVE PRESSURE DECAY IN POLYCARBONATE TARGETS
IMPACTED BY CYLINDRICAL POLYCARBONATE PROJECTILES

By John D. Di Battista
Langley Research Center

SUMMARY

The shock-wave pressure decay along the impact axis has been obtained as a function of the shock-wave depth in polycarbonate targets, impacted at 6.4 and 7.4 km/sec, with cylindrical polycarbonate projectiles having fineness ratios of 0.715. The shock-wave pressure as a function of the shock-wave depth was obtained by impacting various thickness targets with similar projectiles. Either the projectile velocity or the maximum spray velocity emanating from the target rear surface was used to obtain the compressed target material particle velocity at the target rear surface just prior to the shock-wave reflection. The shock-wave pressure associated with the compressed material particle velocity was computed by using the second Rankine-Hugoniot jump condition across a shock and a quadratic relation between compressed material particle velocity and shock-wave velocity.

For the projectile impacts at 6.4 and 7.4 km/sec, the shock-wave pressure at the impact axis remained constant at 0.282×10^{11} and 0.355×10^{11} newtons/m², respectively, for a shock-wave penetration near 75 percent of the projectile radius. Near this penetration the rarefaction wave, originating from the free boundary of the interface between the target and projectile, arrived at the impact axis, and the shock-wave pressure began to decrease rapidly and reached pressures near 0.085×10^{11} and 0.110×10^{11} newtons/m² at shock-wave penetrations near 3.10 and 3.30 projectile radii, respectively. At these penetration depths, the shock-wave pressure began decreasing even more rapidly because of a rarefaction wave which originated at the projectile rear surface and the shock-wave pressures became inversely proportional to the shock-wave penetration raised to approximately the 2.5 power for shock-wave penetrations as great as 7.0 projectile radii.

Experimental data on the transient shock-wave phenomena were taken in low sound speed targets which could be impacted at hypervelocities with cylinders of like material using conventional light gas guns. The data presented herein are useful for comparison with results of hydrodynamic numerical calculations. The projectile launching, detecting, and photographing techniques along with target placement used to obtain unskewed cylindrical projectile impacts are fully described.

INTRODUCTION

The impacts of meteoroids having velocities greater than 20 km/sec cannot, presently, be simulated in the laboratory; thus, the damage to expect from such impacts on spacecraft materials such as aluminum and steel cannot be experimentally observed. Numerical solutions of such hypervelocity impact problems have been generated by Bjork (ref. 1), Riney and Heyda (ref. 2), and Walsh and Johnson (ref. 3). These solutions describe the transient shock-wave phenomena in targets and provide methods for determining final crater dimensions. Initially, these solutions were used to investigate the case of a moderate fineness ratio (length/diameter) cylindrical projectile impacting a like material target. At present, little experimental data on such impacts with the transient shock-wave phenomena being monitored have been published. Experimental data on the transient shock-wave phenomena produced in low-sound-speed targets impacted at hypervelocities by cylinders of like material are presented herein for possible comparison with the results of these hydrodynamic numerical calculations.

A technique, which involved placing the targets very close to the muzzle of the gun and leaving only a very short unrestrained projectile flight path, was used to obtain unskewed cylindrical projectile impacts. A material having a very low speed of sound was selected for the targets and projectiles in order to create hypervelocity impacts with the velocity capability of the light gas gun used. Targets of various thickness were impacted with similar projectiles to establish the shock-wave pressure decay as a function of shock-wave depth in the target. Either the projectile velocity or the maximum spray velocity emanating from the rear surface of various thickness targets is used to obtain the compressed target material particle velocity at the target rear surface just prior to the shock-wave reflection. The compressed material particle velocity is taken as one-half the maximum spray velocity or one-half of the projectile velocity, depending on the one used. The shock-wave pressure associated with the compressed material particle velocity is computed from the second Rankine-Hugoniot jump condition across a shock with the use of a quadratic relation between compressed material particle velocity and shock-wave velocity.

SYMBOLS

p pressure, newtons/m²

r radius, cm

U velocity, km/sec

ρ	density, gm/cm ³
C_1	empirical constant in equation (2), 2.71 km/sec
C_2	empirical constant in equation (2), 1.568 dimensionless
C_3	empirical constant in equation (2), -0.37×10^{-1} sec/km

Subscripts:

c	shock-compressed material
o	undisturbed material
p	projectile
s	shock wave
t	target spray
1,2	denotes different time values

PROJECTILES AND TARGETS

Polycarbonate projectiles and targets having a density of 1.2 grams/cm³ were used in the impact tests. Polycarbonate was chosen because it has a low speed of sound, approximately 2.7 km/sec in the uncompressed material, and a high impact strength to withstand the high light-gas-gun launch pressures. This material property combination makes possible, with the use of current light gas guns, similar material test impacts at impact Mach numbers greater than 2.5.

The projectiles were cylinders which weighed 0.122 gram \pm 0.012 and had fineness ratios of 0.715. The projectile diameter was 0.568 cm \pm 0.0142 and length was 0.406 cm \pm 0.0142.

The target thicknesses were approximately 0.05, 0.100, 0.170, 0.200, 0.250, 0.320, 0.480, 0.650, 0.800, 0.980, 1.270, and 1.900 cm. The targets were 7.0 cm square.

TEST SETUP AND OPERATION

Figure 1 is a schematic of the test setup. An accelerated reservoir hydrogen gas gun similar to that developed by Curtis (ref. 4) was used to launch the projectiles at velocities of 6.4 ± 0.4 and 7.4 ± 0.5 km/sec. The light-gas gun muzzle was attached to an evacuated rectangular test chamber which had transparent methyl methacrylate windows through which projectile and target material spray photographs were taken. The internal dimensions of the test chamber are $7.6 \times 7.6 \times 33$ cm. Mounted in the test chamber between the gun muzzle and target is a baffle which deflects the gun muzzle gases away from the flight path of the projectile. As seen in the schematic, the target was placed between 15 and 25 centimeters from the gun muzzle. By placing the target close to the gun muzzle, the projectile, which is sufficiently long to resist tilting in the gun barrel, does not have a long unrestrained flight path in which to tilt. A series of backlit photographs of the projectile traveling toward the target and of the spray front emanating from the target rear surface were obtained with a high-speed framing camera. Since the flight path is short, very little projectile dispersion can occur, and the camera field of view can be narrowed to obtain maximum detail. The projectile and spray front velocities were calculated by dividing the distance traveled between photographs by the time elapsed between photographs. The framing camera used was a continuous writing type. A xenon flash tube which had a light discharge duration of 60μ sec provided the back-lighting for the photographs. The time at which the photographs were taken was controlled by a phototube detecting the first gun muzzle light. This sequencing technique proved to be extremely simple and reliable in operation.

ANALYTICAL DEVELOPMENT

During a hypervelocity impact, the projectile energy is transferred to the target material by a strong shock wave which precedes the projectile into the target. Figure 2 shows the shock wave at several depths as it propagates into the target material. The shock-wave velocity U_S and the shock-wave pressure p_S and the compressed material particle velocity U_C associated with an element of compressed material immediately behind the shock wave and along the axis of impact are designated at each shock-wave position. As the shock wave propagates into the target, it is attenuated by rarefaction waves which originate at the projectile boundaries and the shock-wave pressure and compressed material particle velocity show a continual decline.

The following method is employed to obtain the shock-wave pressure at the impact axis. The second Rankine-Hugoniot jump condition across a shock wave

$$p_S = \rho_0 U_S U_C \quad (1)$$

is used to relate the shock-wave pressure p_s to the product of the original target material density ρ_0 , the shock-wave velocity, and the compressed material particle velocity. A relationship between the shock-wave velocity and the compressed material particle velocity is given by the quadratic equation:

$$U_s = C_1 + C_2 U_c + C_3 U_c^2 \quad (2)$$

where C_1 , C_2 , and C_3 are constants which were empirically determined for methyl methacrylate in reference 5. The shock-wave pressure of those tests was 0.100×10^{11} newtons/m². The use of equation (2) and the same constants to compute the shock-wave velocities in the polycarbonate material of the present tests up to the higher shock-wave pressure of 0.387×10^{11} newtons/m² is felt to be justified since both materials are plastics with approximately the same density and sound speed in the uncompressed state and the accuracy of the extrapolated curve is felt to be within the accuracy of the experimental technique used in experiments reported here. By combining equations (1) and (2), an equation which relates the shock-wave pressure to the compressed material particle velocity is obtained in the form:

$$p_s = \rho_0 (C_1 U_c + C_2 U_c^2 + C_3 U_c^3) \quad (3)$$

The values of the compressed material particle velocity can be determined from experiments. The initial shock-wave propagation along the axis of impact is one dimensional. By noting the symmetry of the impact situation which exists between a like material projectile and target, the compressed material particle velocity is related to the impacting projectile velocity U_p as follows:

$$U_c = U_p/2 \quad (4)$$

Later, as the shock wave penetrates deeper into the target, shock-wave attenuation occurs because of the arrival at the shock front of rarefaction waves originating at the projectile boundaries. (See fig. 2.) The maximum velocity of material emanating from the targets rear surface U_t can be related to the compressed material particle velocity through an elastic analysis giving

$$U_c = U_t/2 \quad (5)$$

To determine the compressed material particle velocity for a specific shock-wave propagation depth, a target having a thickness equal to that depth must be impacted and

the spray observed as illustrated in figure 3. In addition, the elimination of the compressed-material particle velocity between equations (4) and (5) predicts that maximum spray velocity should be equal to the projectile impact velocity during one-dimensional shock-wave penetration. Any large increase in the maximum spray velocity over the projectile impact velocity would indicate that the elastic analysis was not valid at that projectile impact velocity and that the target material was returning from the shocked state to zero pressure with sufficient internal energy release to cause heating, melting, and vaporization of target material. Also, material decomposition could occur. With such phenomena occurring at the target rear surface upon material expansion from the shocked state, equation (5) would contain an error at this shock-wave pressure.

RESULTS AND DISCUSSION

Table I contains all the experimentally obtained data from each test and the calculated shock-wave pressure at the impact axis. A double asterisk on either the projectile velocity or the maximum spray velocity indicates the value used in the pressure calculations. The ratio of maximum spray velocity and projectile velocity for the two impact velocities tested is plotted as a function of the target thickness in figures 4 and 5.

Three distinct regions of maximum spray velocity variation with increasing target thickness can be noted. For targets thinner than $0.75r_p$, where r_p represents projectile radii, the maximum spray velocity did not vary at the impact axis; thus, the shock wave was unchanged before reaching the target rear surface.

For targets thicker than $0.75r_p$, the target material spray velocity began decreasing with increasing target thickness. This decrease indicates the attenuation of the shock wave at the impact axis by a rarefaction wave originating at the free boundary of the interface between the target and the projectile. It should be noted that this value of $0.75r_p$ is about one-half the result obtained by Al'Tshuler et al. (ref. 6).

For targets thicker than approximately $3.0r_p$ the target material spray velocity began decreasing at a very rapid rate with increasing target thickness because of the arrival of a rarefaction wave originating at the projectile rear surface.

For the two impact cases of the test, the calculated shock-wave pressures are plotted as a function of shock-wave depth in figures 6 and 7. To obtain the initial shock-wave pressure which is produced during the one-dimensional shock-wave penetration at the impact axis in the targets, the projectile velocity is used with equations (3) and (4). The horizontal lines in figures 6 and 7 which are drawn at pressures of 0.282×10^{11} and 0.355×10^{11} newtons/m² in the unattenuated shock-wave region out to $0.75r_p$ were calculated by assuming impact velocities of exactly 6.4 and 7.4 km/sec, respectively. The circles in this region are the pressures calculated with the use of in each case the actual

TABLE I.- EXPERIMENTAL DATA AND CALCULATED PRESSURES FOR A CYLINDRICAL
POLYCARBONATE PROJECTILE IMPACTING A POLYCARBONATE TARGET
[Length, 0.406 cm; diameter, 0.568 cm]

Shot number	Target thickness, cm	Projectile velocity, km/sec	Maximum spray velocity, km/sec	Shock-wave pressure, newtons/m ²
1	0.056	**7.66	9.36	0.376×10^{11}
2	.056	**7.47	9.88	.361
3	.109	**7.10	8.88	.332
4	.107	**7.04	9.50	.328
5	.174	**7.80	10.57	.387
6	.211	7.12	*7.46	
7	.252	7.12	*6.63	
8	.333	7.56	**6.45	.286
9	.333	7.18	**5.89	.248
10	.492	7.78	**5.38	.215
11	.635	7.15	**3.86	.129
12	.635	7.06	**3.53	.113
13	.793	7.09	**3.47	.111
14	.971	7.09	**3.03	.091
15	1.285	7.25	**1.50	.035
16	1.933	7.85	**.85	.017
17	.053	**6.22	7.55	.270
18	.104	**6.30	6.43	.275
19	.203	**6.14	6.39	.264
20	.252	6.48	**5.47	.221
21	.318	6.55	**4.72	.176
22	.328	6.01	**4.46	.161
23	.333	6.38	**4.69	.174
24	.493	6.73	**4.23	.149
25	.495	6.78	**3.96	.127
26	.645	6.66	**3.44	.109
27	.800	6.33	**3.02	.090
28	.968	6.19	**2.52	.070
29	1.270	6.77	**1.45	.033
30	1.284	6.72	**1.43	.033
31	1.285	6.16	**1.22	.027
32	1.988	6.62	**.59	.011

*Shock-wave pressure is not calculated because compressed material particle velocity could not be obtained from either the projectile or maximum spray velocity.

**Value used in pressure calculations.

projectile impact velocity which, as already discussed, was within ± 6 percent of either 6.4 or 7.4 km/sec. The initial target material density ρ_0 was taken as 1.20 gm/cm³.

For the 6.4 km/sec impacts into the target thicknesses greater than 0.75r_p, the compressed material particle velocity was calculated with the use of equation (5). Shots 18 and 19 for which the spray velocity was approximately equal to the projectile velocity indicated that this procedure would be permissible. When equation (5) is used with equation (3), the shock-wave pressures less than 0.282×10^{11} newtons/m² are calculated for the shots 20 to 32 and are plotted as circles in figure 7. A curve has been faired through the data points from 0.75r_p to 3.10r_p where the shock-wave pressure has decayed to 0.085×10^{11} newtons/m². At 3.10r_p a discontinuous change in the rate of shock-wave decay occurred because of the arrival of a rarefaction wave originating at the projectile rear surface. A straight line was drawn from 3.10r_p to 7.00r_p where the shock-wave pressure appeared to decrease inversely with increasing shock-wave depth to approximately the 2.5 power.

For the 7.4 km/sec impacts, the maximum spray velocity was well in excess of the projectile impact velocity for all shots during the initial one-dimensional shock-wave penetration along the impact axis in the targets. The maximum spray velocity was typically 1.3 times the projectile impact velocity. This increase of the maximum spray velocity over the projectile impact velocity showed that irreversible heating and possible material decomposition had occurred. To avoid using values of compressed material particle velocity computed from equation (5) when such a situation occurs, only shots 8 to 16 where maximum spray velocity was less than 6.4 km/sec, are used to compute the pressure points plotted in figure 7 for the shock-wave depths greater than 0.75r_p. The sole exception to this, shot 8, with a velocity of 6.45 km/sec, has an error bar of minus 20 percent attached to the plotted pressure point to account for any possible irreversible heating or material decomposition affecting the value of the maximum spray velocity.

A solid line has been drawn on figure 7 through the data from 0.75 to 3.30r_p where the shock-wave pressure has decayed to 0.110×10^{11} newtons/m². From 3.30 to 7.00r_p the shock-wave pressure again appeared to decay inversely with shock-wave depth raised to approximately the 2.5 power.

Figure 8 shows the change in spray cloud shape occurring when the target thickness was varied while the shock wave was still unattenuated at the impact axis in the target. Although the ratio of maximum spray velocity and projectile velocity remained constant the spray cloud shape did not. In part (a) of figure 8 which shows a 7.4 km/sec impact into a target having a thickness equal to 0.198r_p, a wide cloud front travels at the maximum spray velocity. In part (b) of figure 8 the target thickness is increased to 0.600r_p and the front of the cloud traveling at maximum velocity has become narrower.

Figure 9(a) shows an example of a spray cloud formed in a target thickness where shock-wave attenuation has occurred at the impact axis because of a rarefaction wave from the free boundary of the interface between the target and projectile. The cloud was formed by an impact at 6.55 km/sec into a target $1.12r_p$ in thickness.

When the maximum spray velocity was less than 3.50 km/sec which occurs in these experiments for targets which have thicknesses greater than $2.5r_p$, the compressed material particle velocity was determined from the velocity of polycarbonate dust particles emanating from the target rear surface. Figure 9(b) is an example of the dust cloud and shows the position of the dust cloud relative to the target rear surface.

CONCLUDING REMARKS

For projectile impacts at 6.4 and 7.4 km/sec the shock-wave pressure at the impact axis remained constant at 0.282×10^{11} and 0.355×10^{11} newtons/m², respectively, to a shock-wave penetration near 75 percent of the projectile radius. It should be noted that the shock-wave penetration $0.75r_p$ to which the shock-wave pressure remained constant was approximately one-half the expected value. Near this shock-wave penetration, the rarefaction wave, originating from the free boundary of the interface between the target and projectile, arrived at the impact axis and the shock-wave pressure rapidly decreased to pressures near 0.085×10^{11} and 0.110×10^{11} newtons/m² at shock-wave penetrations near 3.10 and 3.30 projectile radii, respectively. At these penetration depths, the shock-wave pressure again decreased because of a rarefaction wave which originated at the projectile rear surface and the shock-wave pressures became inversely proportional to the shock-wave penetration raised to approximately the 2.5 power for shock-wave penetrations as great as 7.0 projectile radii.

For projectile impacts at 7.4 km/sec into target thicknesses less than 75 percent of the projectile radius, the maximum spray velocity was typically 1.3 times the projectile velocity. This result showed that the spray velocity component acquired during expansion could not be approximated as equal to the velocity component acquired during shock-wave compression at a shock-wave pressure of 0.355×10^{11} newtons/m².

Langley Research Center,
National Aeronautics and Space Administration,
Langley Station, Hampton, Va., February 26, 1968,
124-09-15-03-23.

REFERENCES

1. Bjork, R. L.: Effects of a Meteoroid Impact on Steel and Aluminum in Space. [Paper] P-1662, The Rand Corp., Dec. 16, 1958.
2. Riney, T. D.; and Heyda, J. F.: Hypervelocity Impact Calculations and Their Correlation with Experiment. Tech. Inform. Ser. No. R64SD64 (Contract No. AF 08(635)-3781), Missile Space Div., Gen. Elec. Co., Sept. 1964.
3. Walsh, J. M.; Johnson, W. E.; Dienes, J. K.; Tillotson, J. H.; and Yates, D. R.: Summary Report on the Theory of Hypervelocity Impact. GA-5119 (Contract DA-04-495-AMC-116(X)), Gen. Dyn., Mar. 31, 1964. (Available from DDC as AD436251.)
4. Curtis, John S.: An Accelerated Reservoir Light-Gas Gun. NASA TN D-1144, 1962.
5. Coleburn, N. L.; and Liddiard, T. P., Jr.: Hugoniot Equations of State of Several Unreacted Explosives. J. Chem. Phys., vol. 44, no. 5, Mar. 1, 1966, pp. 1929-1936.
6. Al'Tshuler, L. V.; Kormer, S. B.; Brazhnik, M. I.; Vladimirov, L. A.; Speranskaya, M. P.; and Funtikov, A. I.: The Isentropic Compressibility of Aluminum, Copper, Lead, and Iron at High Pressures. Soviet Phys. JETP, vol. 11, no. 4, Oct. 1960, pp. 766-775.

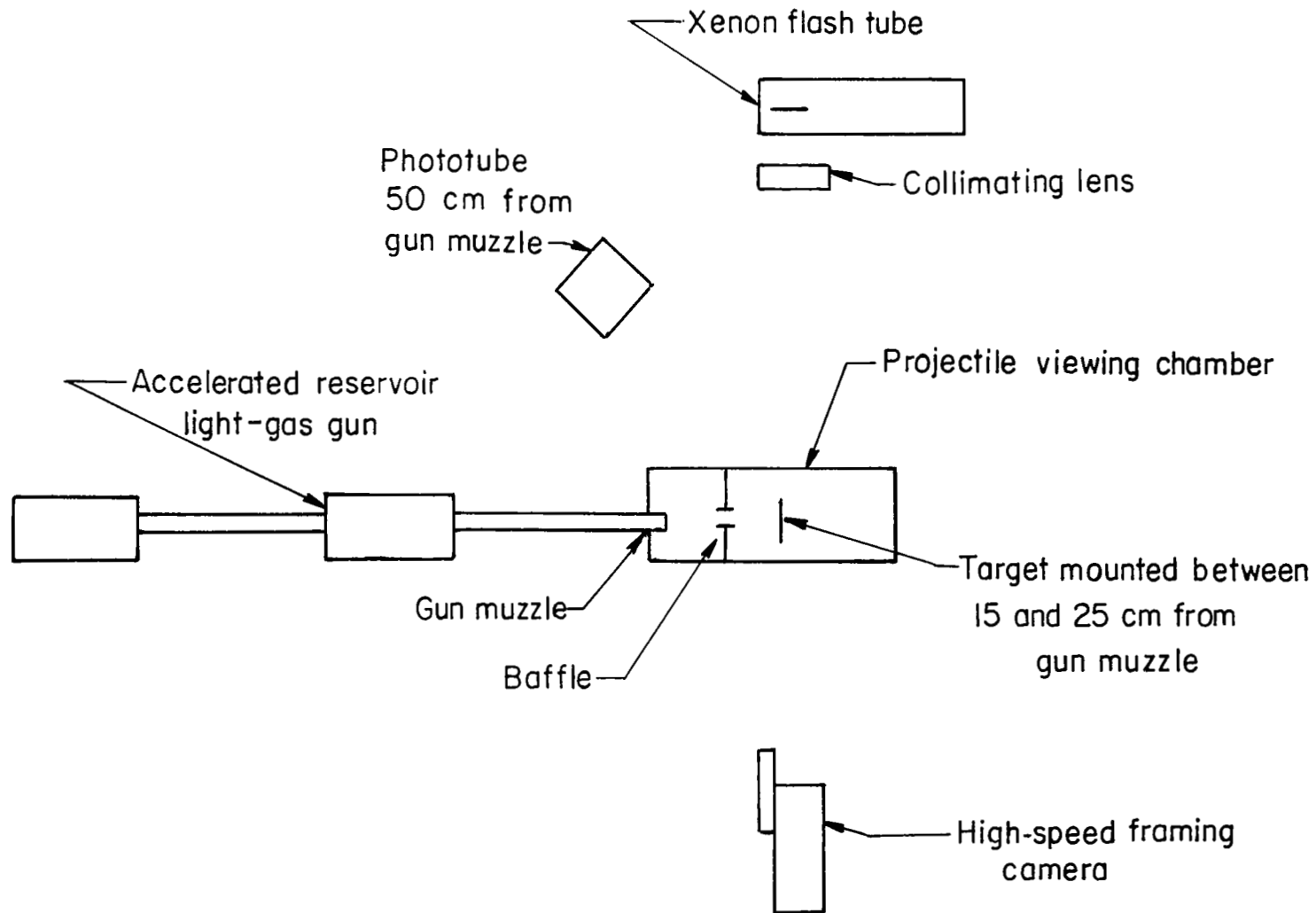


Figure 1.- Schematic of test setup.

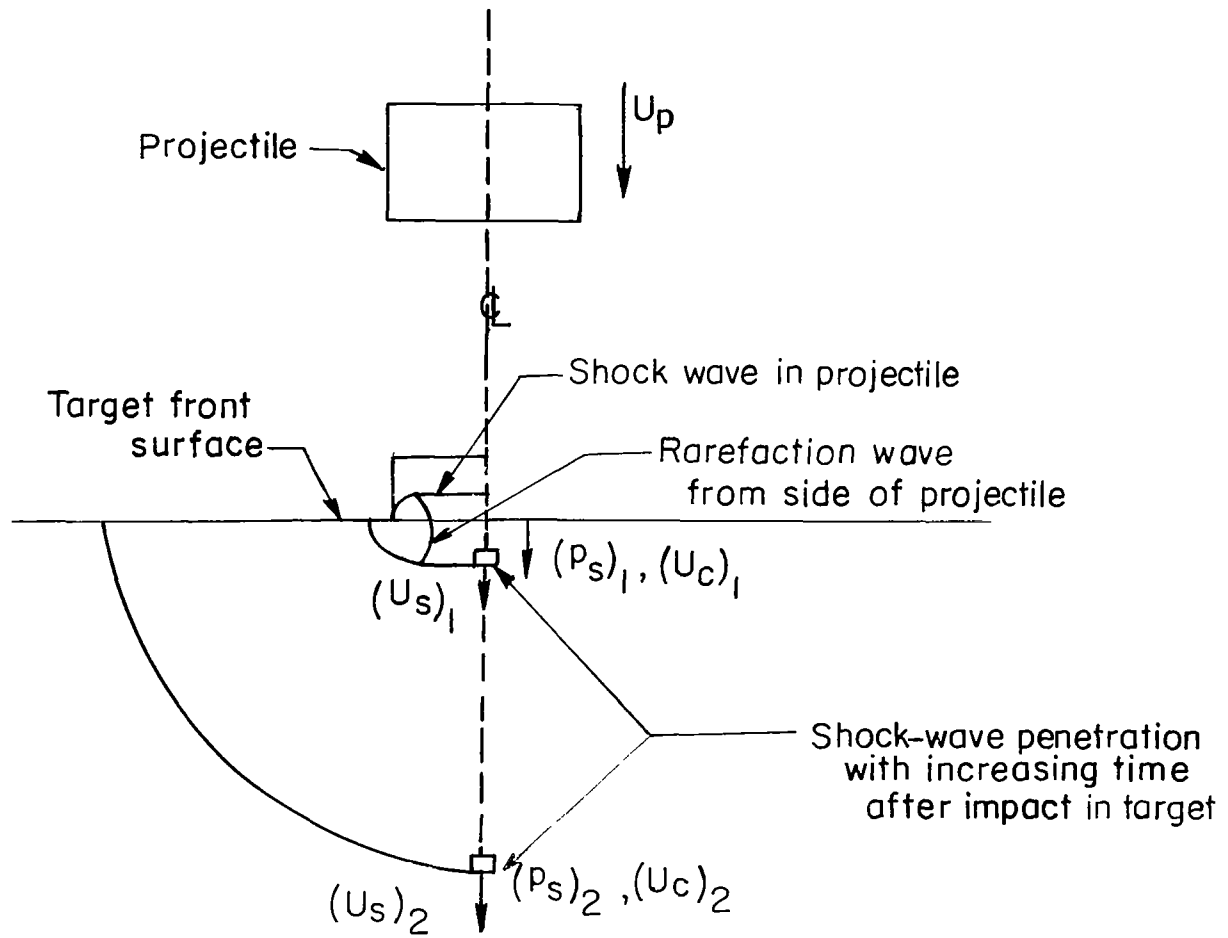


Figure 2.- Shock wave shown in the target at several different positions. Where $(U_s)_1 > (U_s)_2$, $(U_c)_1 > (U_c)_2$, $(P_s)_1 > (P_s)_2$.

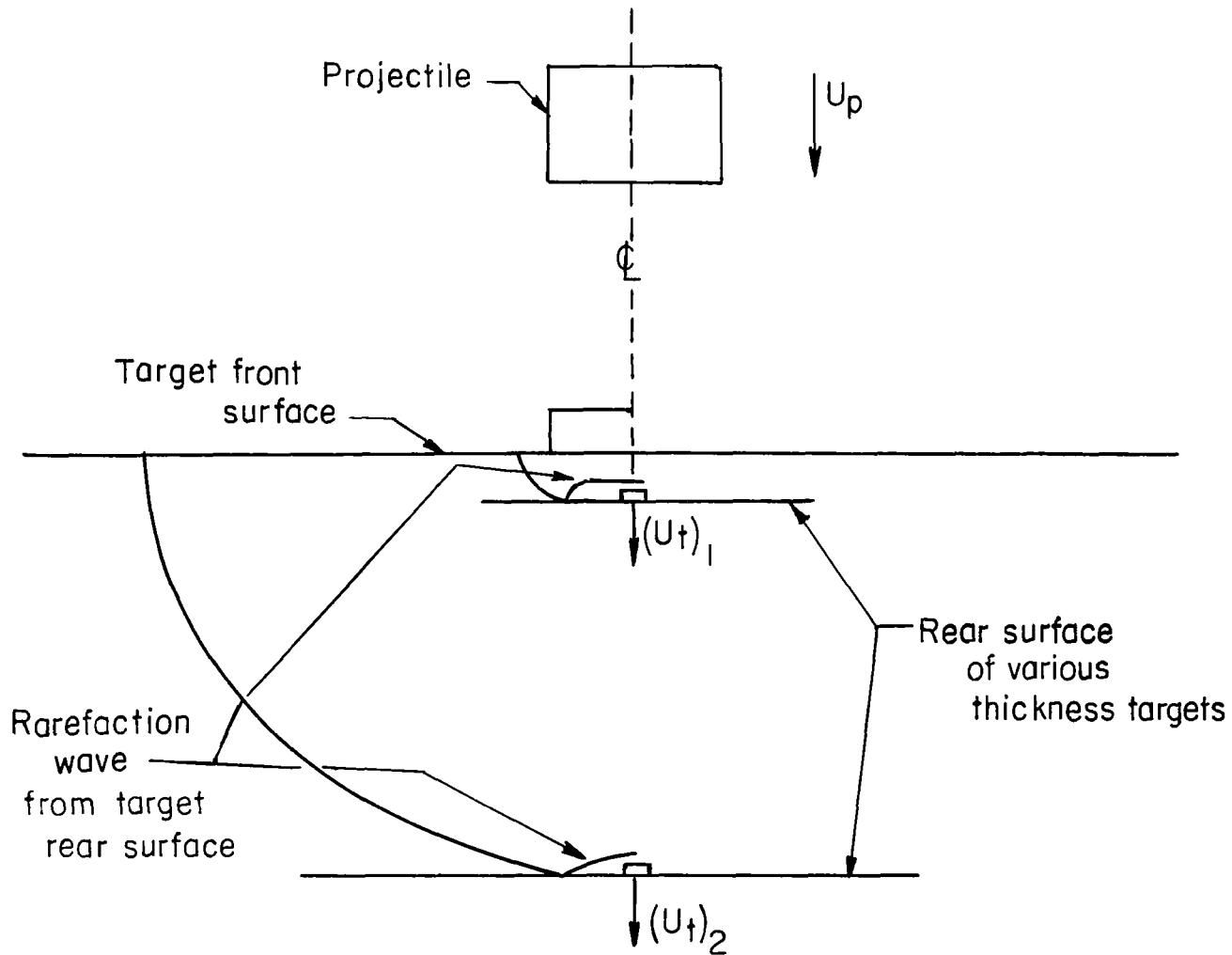


Figure 3.- Conditions at target rear surface just after shock-wave reflection as rarefaction wave. Where $(U_t)_1 > (U_t)_2$.

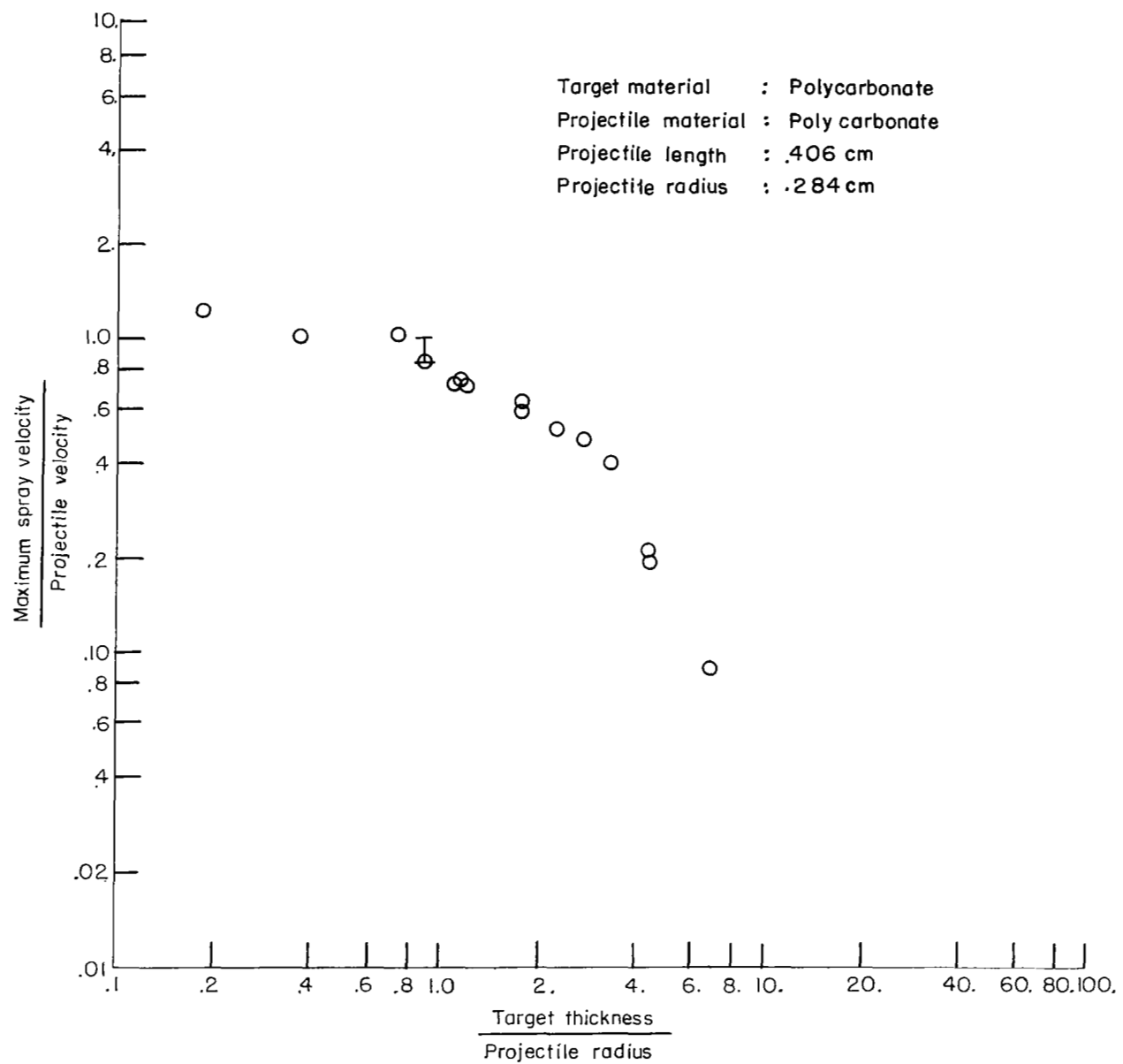


Figure 4.- Maximum spray velocity as a function of target thickness for impact at 6.4 km/sec.
 Error bar attached to value to account for difficulty in determining maximum spray velocity.

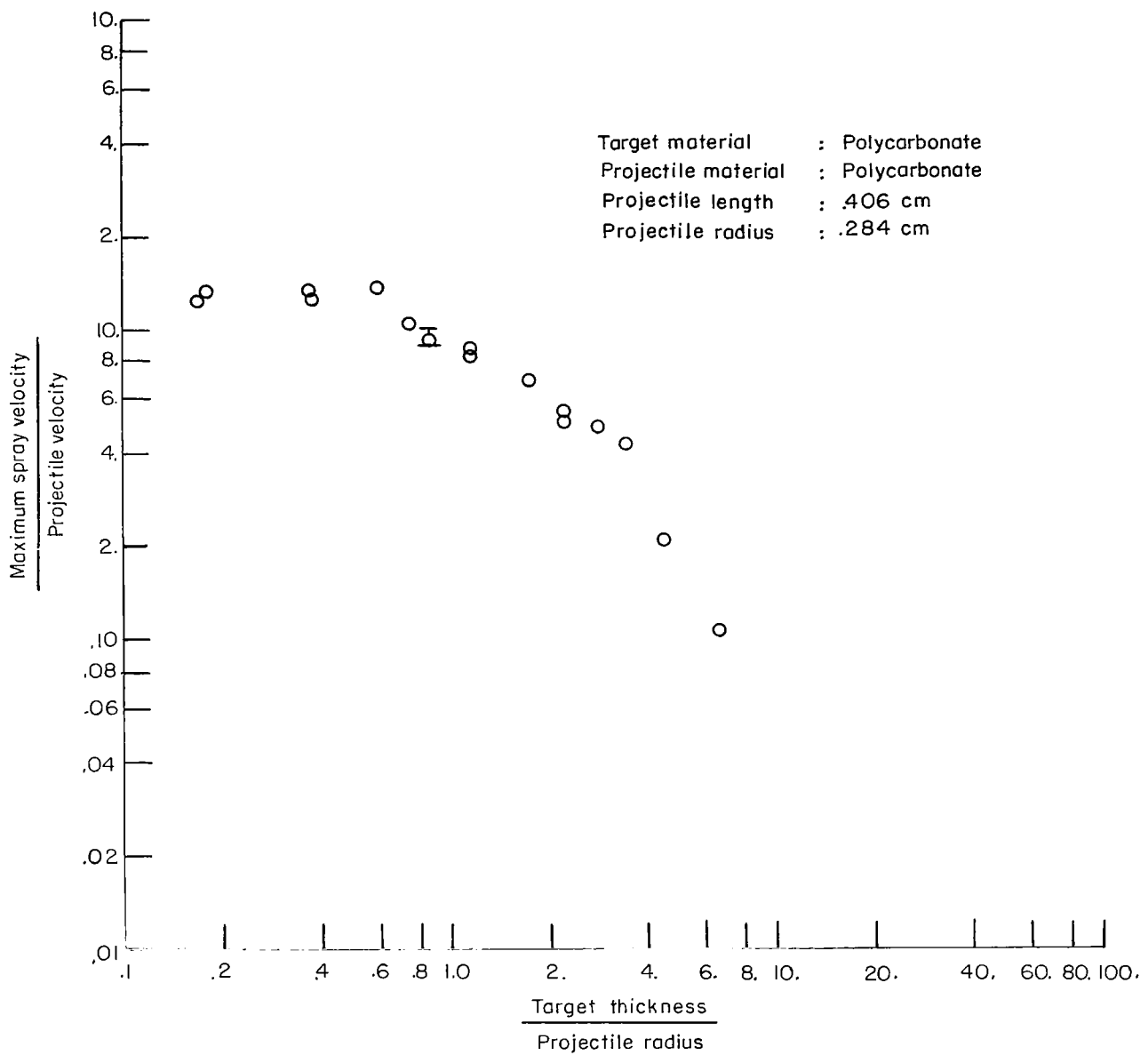


Figure 5.- Maximum spray velocity as a function of target thickness for impact at 7.4 km/sec.
 Error bar attached to value to account for difficulty in determining maximum spray velocity.

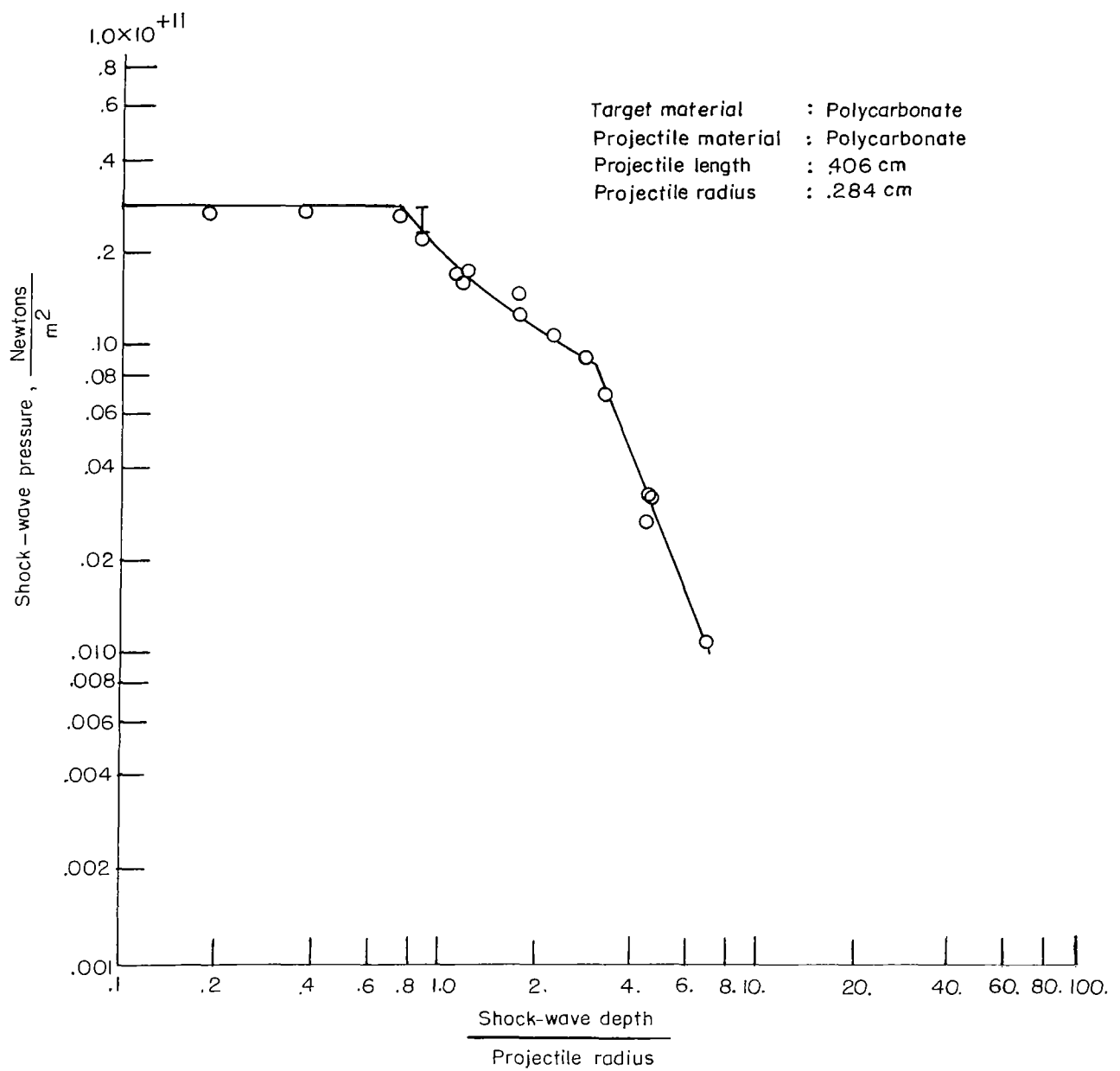


Figure 6.- Shock-wave pressure as a function of shock-wave depth for impact at 6.4 km/sec.

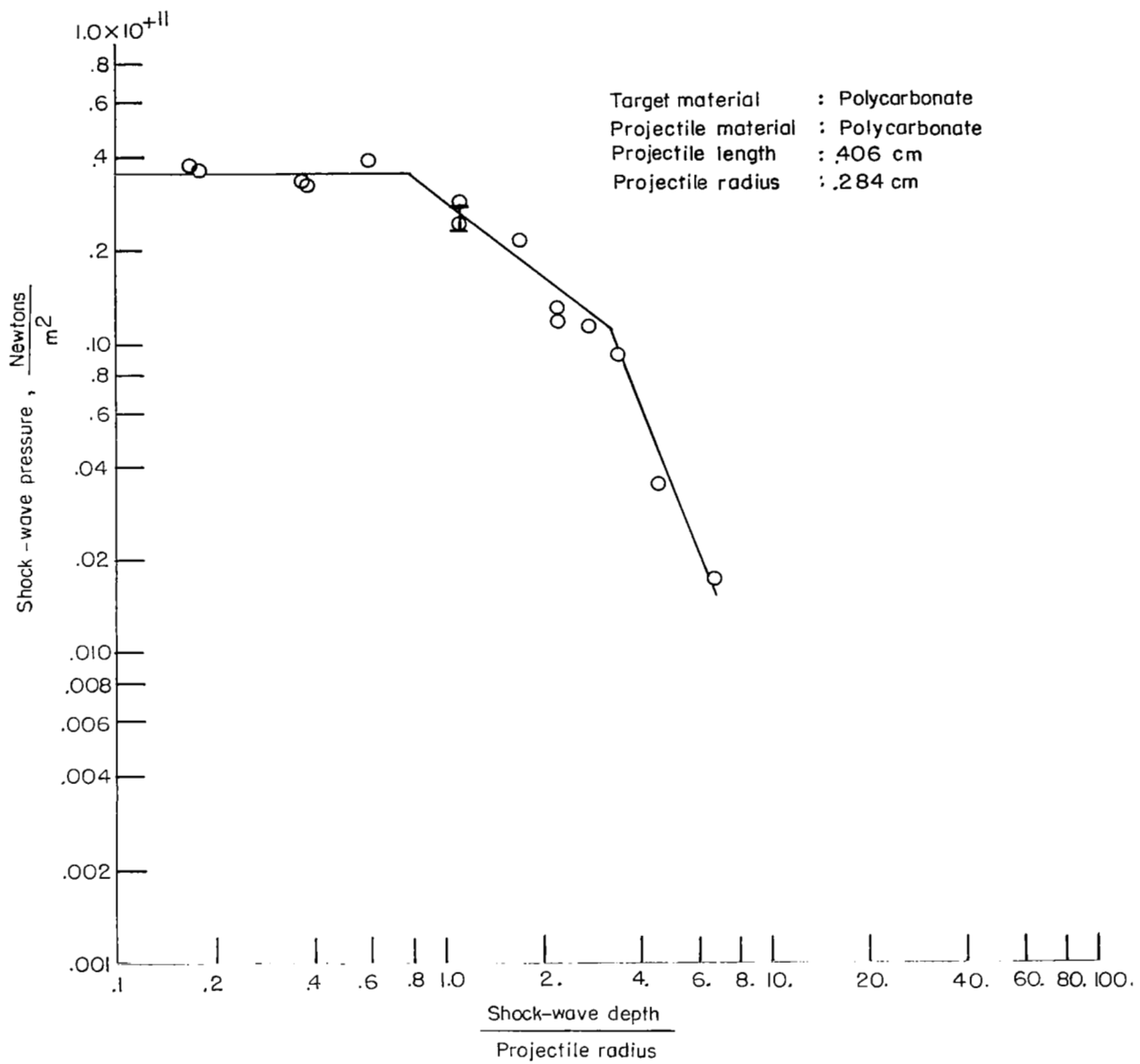
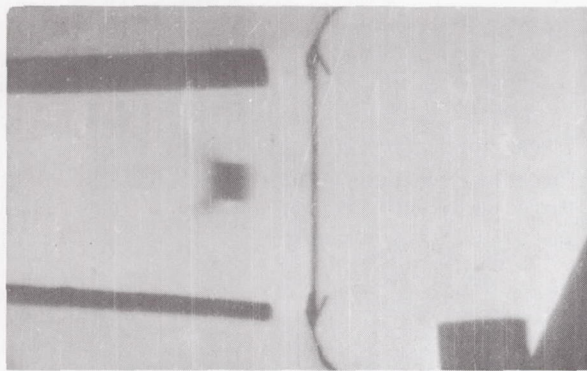
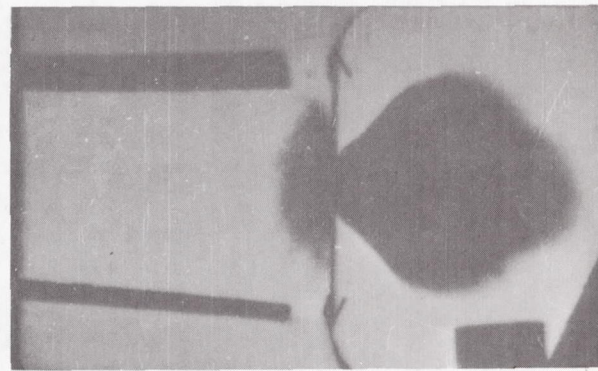


Figure 7.- Shock-wave pressure as a function of shock-wave depth for impact at 7.4 km/sec.



$-.91 \mu\text{sec}$

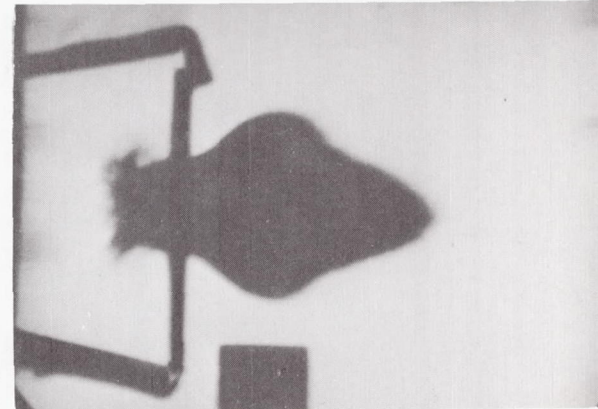


$3.64 \mu\text{sec}$

(a) Shot 2.



$-.91 \mu\text{sec}$

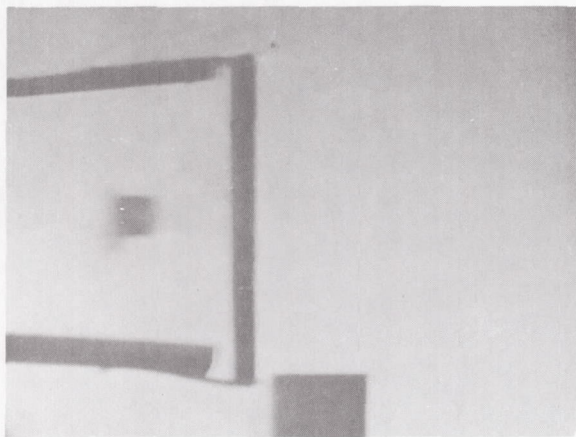


$3.64 \mu\text{sec}$

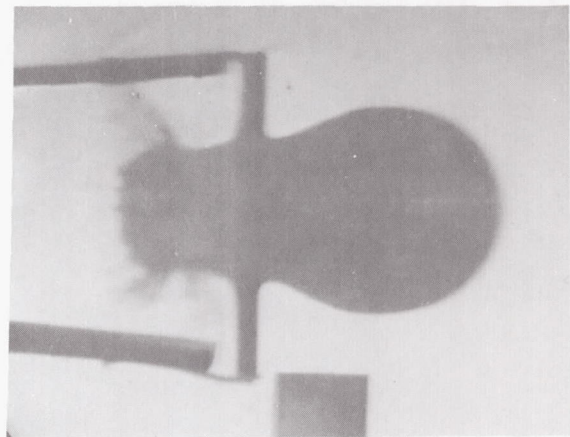
(b) Shot 5.

Figure 8.- Variation in spray cloud shape with target thickness.

L-68-847

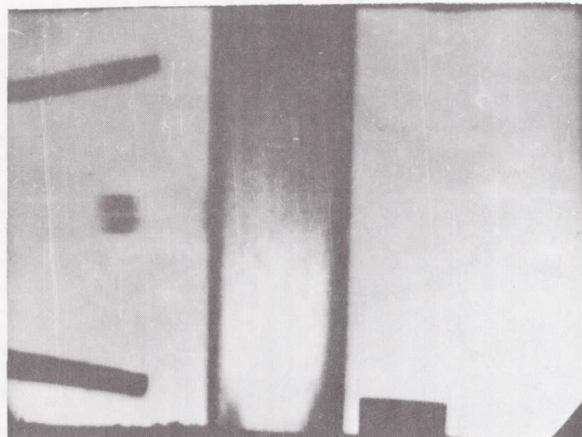


-1.84 μ sec

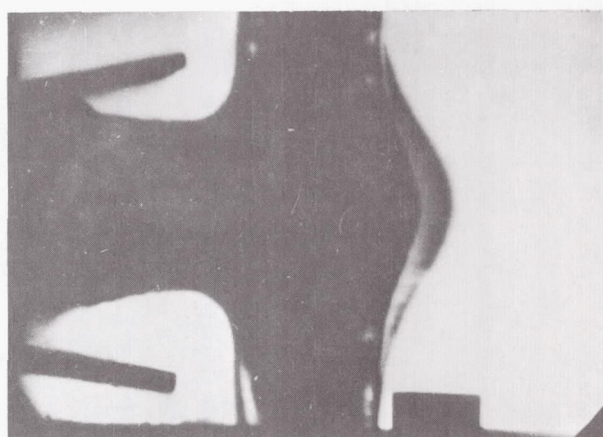


6.44 μ sec

(a) Shot 21.



-.90 μ sec



16.73 μ sec

(b) Shot 16.

Figure 9.- Two spray profiles from two thickness targets.

L-68-848

NATIONAL AERONAUTICS AND SPACE ADMINISTRATION
WASHINGTON, D. C. 20546
OFFICIAL BUSINESS

FIRST CLASS MAIL

POSTAGE AND FEES PAID
NATIONAL AERONAUTICS AND
SPACE ADMINISTRATION

010014701305 66235 00903
AERONAUTICS AND SPACE LABORATORY/AFSC/AF
SAC/TECHNICAL INFORMATION DIVISION, MEXICO 87117

TECHNICAL INFORMATION DIVISION, MEXICO CITY, D.F. 11

POSTMASTER: If Undeliverable (Section 158
Postal Manual) Do Not Return

"The aeronautical and space activities of the United States shall be conducted so as to contribute . . . to the expansion of human knowledge of phenomena in the atmosphere and space. The Administration shall provide for the widest practicable and appropriate dissemination of information concerning its activities and the results thereof."

— NATIONAL AERONAUTICS AND SPACE ACT OF 1958

NASA SCIENTIFIC AND TECHNICAL PUBLICATIONS

TECHNICAL REPORTS: Scientific and technical information considered important, complete, and a lasting contribution to existing knowledge.

TECHNICAL NOTES: Information less broad in scope but nevertheless of importance as a contribution to existing knowledge.

TECHNICAL MEMORANDUMS: Information receiving limited distribution because of preliminary data, security classification, or other reasons.

CONTRACTOR REPORTS: Scientific and technical information generated under a NASA contract or grant and considered an important contribution to existing knowledge.

TECHNICAL TRANSLATIONS: Information published in a foreign language considered to merit NASA distribution in English.

SPECIAL PUBLICATIONS: Information derived from or of value to NASA activities. Publications include conference proceedings, monographs, data compilations, handbooks, sourcebooks, and special bibliographies.

TECHNOLOGY UTILIZATION PUBLICATIONS: Information on technology used by NASA that may be of particular interest in commercial and other non-aerospace applications. Publications include Tech Briefs, Technology Utilization Reports and Notes, and Technology Surveys.

Details on the availability of these publications may be obtained from:

SCIENTIFIC AND TECHNICAL INFORMATION DIVISION
NATIONAL AERONAUTICS AND SPACE ADMINISTRATION
Washington, D.C. 20546